

Automated segmentation of retinal pigment epithelium cells in fluorescence adaptive optics images

Piero Rangel-Fonseca,^{1,*} Armando Gómez-Vieyra,² Daniel Malacara-Hernández,¹ Mario C. Wilson,³ David R. Williams,^{4,5} and Ethan A. Rossi⁵

¹Centro de Investigaciones en Óptica, Loma del Bosque 115, Lomas del Campestre, León, Gto. 37150, Mexico

²Laboratorio de Sistemas Complejos, Departamento de Ciencias Básicas, Universidad Autónoma Metropolitana, Unidad Azcapotzalco, Av. San Pablo 180, Azcapotzalco, D.F. 02200, Mexico

³Laboratoire de Physique des Lasers, Atomes et Molécules, UMR-CNRS 8523, Université Lille 1, 59655 Villeneuve d'Ascq Cedex, France

⁴The Institute of Optics, University of Rochester, 275 Hutchison Rd., Rochester, New York 14642, USA

⁵Center for Visual Science, University of Rochester, 601 Elmwood Ave., Rochester, New York 14642, USA

*Corresponding author: piero@laviria.org

Received September 5, 2013; revised November 4, 2013; accepted November 5, 2013;
posted November 5, 2013 (Doc. ID 197068); published November 21, 2013

Adaptive optics (AO) imaging methods allow the histological characteristics of retinal cell mosaics, such as photoreceptors and retinal pigment epithelium (RPE) cells, to be studied *in vivo*. The high-resolution images obtained with ophthalmic AO imaging devices are rich with information that is difficult and/or tedious to quantify using manual methods. Thus, robust, automated analysis tools that can provide reproducible quantitative information about the cellular mosaics under examination are required. Automated algorithms have been developed to detect the position of individual photoreceptor cells; however, most of these methods are not well suited for characterizing the RPE mosaic. We have developed an algorithm for RPE cell segmentation and show its performance here on simulated and real fluorescence AO images of the RPE mosaic. Algorithm performance was compared to manual cell identification and yielded better than 91% correspondence. This method can be used to segment RPE cells for morphometric analysis of the RPE mosaic and speed the analysis of both healthy and diseased RPE mosaics. © 2013 Optical Society of America

OCIS codes: (100.2000) Digital image processing; (100.2960) Image analysis; (100.4995) Pattern recognition, metrics; (110.1080) Active or adaptive optics; (170.4460) Ophthalmic optics and devices; (330.4300) Vision system - noninvasive assessment.

<http://dx.doi.org/10.1364/JOSAA.30.002595>

1. INTRODUCTION

Adaptive optics (AO) retinal imaging methods allow microscopic features, such as individual cells, to be examined *in vivo*, and have become an important tool for the study of retinal diseases [1–11]. The cone photoreceptor mosaic has received the most attention by investigators using AO; cones were the first cells to be imaged in the living eye and are the most accessible to imaging [1,12]. Comparatively little work has focused on retinal pigment epithelium (RPE) cells, which are vital for the maintenance of visual function [13–16], and are implicated in many retinal diseases, such as age-related macular degeneration and cone-rod dystrophy [4,17–19]. The RPE is also a target for therapeutic interventions aimed at restoring visual function, so the ability to examine RPE cell morphology *in vivo* could be important for evaluating the efficacy of these therapies. Morgan *et al.* demonstrated in 2008 that the human RPE mosaic could be imaged using fluorescence AO imaging methods [6]. However, the RPE mosaic has proved challenging for routine imaging in humans. New methods developed at the University of Rochester have recently improved the efficiency of fluorescence imaging of the human RPE in diseased eyes [20]. Recent reports also show that the RPE is accessible to imaging using dark field

imaging methods [21]. However, these technical achievements improving our ability to image the RPE cell mosaic must be coupled with robust analysis tools for large-scale meaningful studies of *in vivo* RPE morphometry to occur.

Accurate detection and classification of patterns in biomedical images is central to identifying and monitoring tissue damage, as well as quantifying its extent. The retinal surface area of interest in clinical or scientific studies can include areas that contain many hundreds to many thousands of individual cells, making manual analysis methods impractical; purely qualitative analysis methods are undesirable for numerous reasons. Hence, it is necessary to have robust and reliable automated methods for classifying and quantifying retinal structures in high-resolution retinal images. Significant progress has been made in this area, but nearly all of it has focused on the development of tools for automatically localizing the position of individual photoreceptor cells [22–24]. Most methods developed to analyze cone mosaics are inappropriate for studying the RPE, as they seek to identify the bright centers of photoreceptor cells, whereas our interest is primarily in segmenting the fluorescent structure in RPE images that defines the borders of adjacent RPE cells. Chiu *et al.* have developed an algorithm for segmenting

RPE cells in confocal microscopy images [23], but we implemented this algorithm and found that it did not perform well on fluorescence AO images due to their higher noise levels. A closed cell segmentation approach is desirable not only because it is important to know how many RPE cells there are in a given retinal area, but also because their morphometry—the shape, size, and spatial arrangement of RPE cells—has been shown in postmortem histological studies to change with aging and disease [16,25–27]. These changes in morphometry may precede cell death and thus it is possible that morphometric changes could be measured before a decrease in the number of cells is observed.

In digital image processing, the most common hurdles to overcome are illumination, scale, and rotation, which are all present in images obtained using AO scanning light ophthalmoscopy (AOSLO). Illumination and scale problems arise from the properties of the optical system [28] and from the characteristics of the microscopic features themselves. Rotation between small AO imaging fields occurs from eye rotation. And just as the brightness of individual photoreceptors can vary in an AO image [5,8,10,29], so too can the fluorescence of individual RPE cells. Since the structure of RPE cells in fluorescence AOSLO images is defined by the fluorescence of individual lipofuscin (and melanolipofuscin) granules within the cell [3,6,19], the shape, size, and distribution of these granules cause variability in the fluorescence of different parts of the cell. In addition, as with other cellular mosaics in the retina, such as the photoreceptors, the RPE cell shape and size vary as a function of eccentricity from the fovea [6,13,14,30,31].

Our approach is related to watershed metallographic and histological image segmentation methods [32–34]. We test our algorithm here on both synthetic and real high-resolution images obtained in both humans and monkeys using several different AOSLO instruments.

2. METHODS

A. Algorithm

The algorithm consists of several stages: (1) smoothing, (2) erosion, (3) edge detection, (4) edge correction, (5) binarization, and (6) shrinking. A schematic diagram of the algorithm is shown in Fig. 1. It was implemented in MATLAB (The MathWorks, Inc., Natick, Massachusetts), using several functions from the Image Processing Toolbox.

Smoothing reduces the noise level in each image; this stage is defined by the convolution $f(x, y) * g(x, y)$ of image $f(x, y)$ and the kernel $g(x, y)$. Let $g(x, y)$ be a circular mean filter; the kernel is shown in Fig. 2(a), [32]. The size of the kernel was selected based on the size of the bright fluorescent zones defining the margin of each cell, with the aim of reducing the noise level without eliminating the cellular structure. If the kernel is too small, the noise level is not reduced significantly, and if the kernel is too large, the cellular structure is eliminated. Figure 3(b) shows the result of the smoothing on the image shown in Fig. 3(a). Smoothing was accomplished through the MATLAB function *conv2*. It should be noted that smoothing results in edge artifacts; this problem was avoided by using large images and cropping the borders after segmentation.

Erosion is the morphological operation described by Serra [34]; it is defined as $a \ominus b$. Let a be the image and let b be the

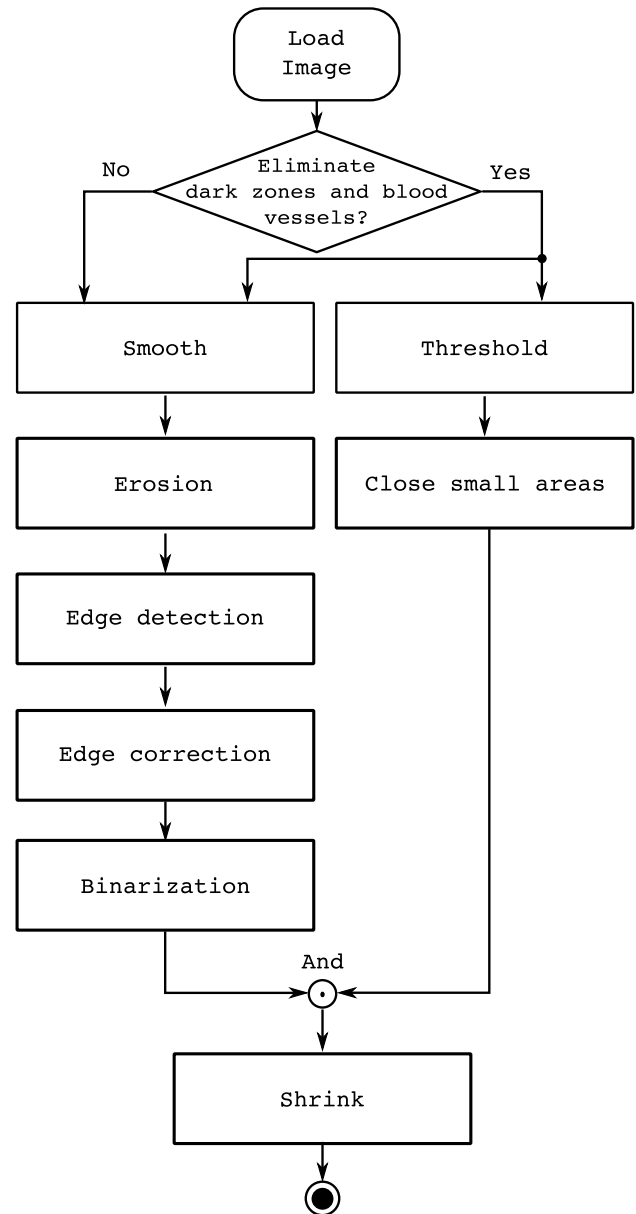


Fig. 1. Schematic representation of the algorithm.

structuring element shown in Fig. 2(b). The structuring element was designed with the goal of shrinking the bright fluorescent zones in the image that define the contours of each RPE cell. Figure 3(c) shows the result of this stage on the image shown in Fig. 3(b). Erosion was implemented using the MATLAB function *imerode*.

Edge detection used the convolution of the image with a Mexican-hat kernel shown in Fig. 2(c). The kernel closely resembles the difference of two Gaussians of Wilson and Giese [33,35,36]. The Mexican-hat kernel was used to detect cell edges. We also tested Laplacian high-pass, Sobel, and Canny filters [33], but found that the Mexican-hat kernel was the most effective. Figure 3(d) shows the result of this stage on the image shown in Fig. 3(c). Edge detection was accomplished using the MATLAB function *conv2*.

Edge correction uses the morphological operation closing $a * b = (a \oplus b) \ominus b$, which is the combination of a dilation followed by an erosion using the same structuring element

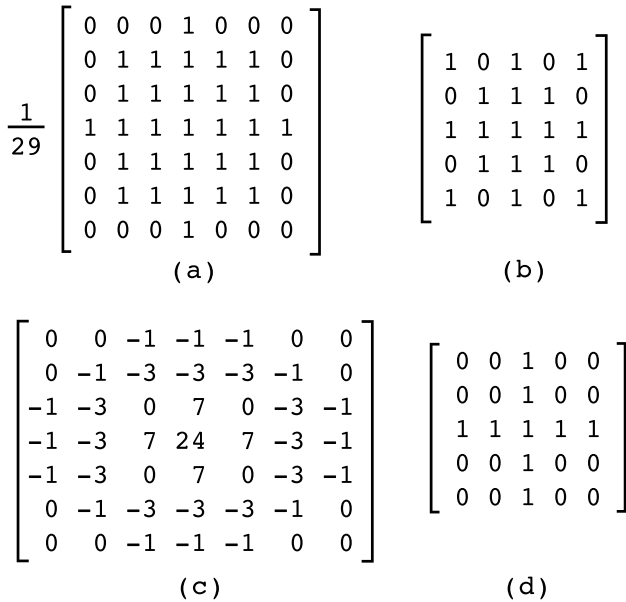


Fig. 2. Kernels used in the algorithm: (a) mean circular filter, (b) structuring element for erosion, (c) Mexican-hat Kernel, and (d) structuring element for edge correction.

[34,37]; it tends to close bright zones and remove dark details from an image with respect to the size and shape of the structuring element [32]. Edge correction uses the structuring element shown in Fig. 2(d); it was designed to correct the edges on the horizontal and vertical directions. Figure 3(e) shows the result of this stage on the image shown in Fig. 3(d). Edge correction was accomplished through the MATLAB function *imclose*.

Binarization is a threshold operation; after using the Mexican-hat kernel, the image contains pixel values below zero, where the zero crossings represent the edge of the cell. Binarization sets all values below one to zero and all values greater than or equal to 1 to 1, as denoted by Eq. (1). Figure 3(f) shows the result of this stage on the image shown in Fig. 3(e):

$$g(x, y) = \begin{cases} 1 & \forall f(x, y) \geq 1 \\ 0 & \forall f(x, y) < 1 \end{cases} \quad (1)$$

Shrinking is the final stage of the algorithm; it is based on the mathematical morphology operators described by Serra [34] and implemented with the MATLAB function *bwmorph*, employing the “shrink” operation. The operation is repeated until the image no longer changes. Shrinking is used to obtain a single pixel contour around each RPE cell. Isolated pixels are then removed using the MATLAB function *bwmorph*, with the “clean” operation. Figure 3(g) shows the result of this final stage on the image shown in Fig. 3(f).

Many fluorescence AO images of the RPE contain dark hypo fluorescent zones, often due to overlying blood vessels or retinal pathology; in some cases it is desirable to remove these areas. Due to the variety of intensity distributions found in fluorescence AO images, we have found that a single method to remove dark zones and blood vessels does not work for all images. Therefore, we propose three different thresholding methods: Huang, Zack, and Otsu [38–40]. Each is appropriate for a different distribution of image intensities that can be determined by inspecting the grayscale histogram. The Huang method was used for the images shown in Fig. 5(c), 5(d) because they exhibit bimodal histograms. For images with dark zones and/or blood vessels without a bimodal histogram, we recommend using one of the other two methods to eliminate these areas. When the image is bright, we suggest using the Otsu method, whereas when the image is dark, we suggest employing the Zack method. The Huang method is based on minimizing the measurement of fuzziness. For this method, thresholding is applied using the Shanon function and the measure of Yager with the Hamming metric [38]. Zack thresholding is based on normalizing the height and dynamic range of the intensity histogram and does not use a fixed offset [39]. The Otsu method used discriminant criterion to maximize the separability of the resultant classes in gray levels [40]. Therefore, to eliminate small dark zones created by thresholding, binary dilations are performed 10

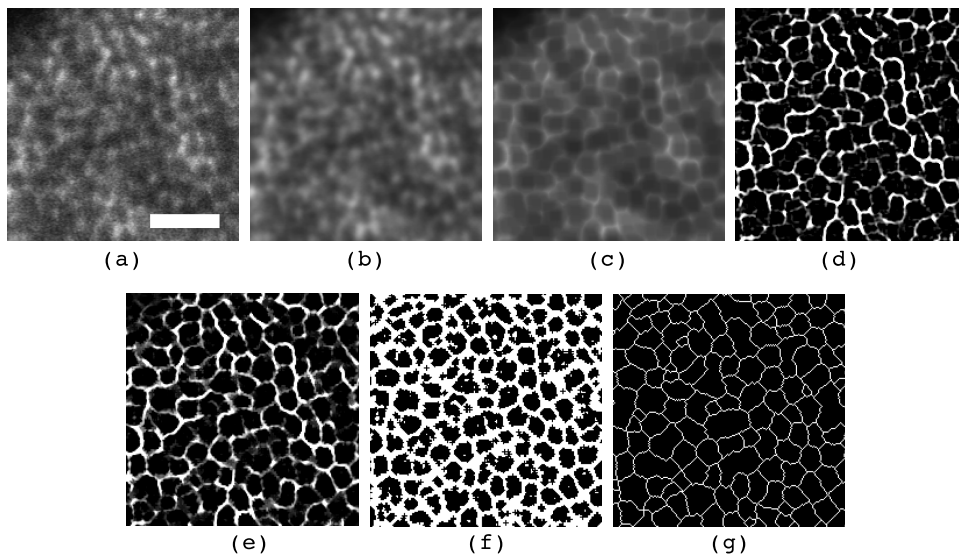


Fig. 3. Stages of the algorithm, human image: (a) original, (b) smoothing, (c) erosion, (d) edge detection, (e) edge correction, (f) binarization, and (g) shrinking. Scale bar: 50 μ m.

times on the image, using a $N8$ structuring element. Dilation was implemented with the MATLAB function *imdilate*.

B. Synthetic Test Images

To validate the algorithm, we tested it on images devoid of RPE structure and on images containing RPE-like structures with known geometry. We tested the algorithm on three different types of synthetic images: (1) white noise, (2) a simulated perfect RPE mosaic, and (3) a simulated noisy RPE mosaic. All synthetic images were created in MATLAB. The white noise image was created using the *rand* MATLAB function to assign a random value to each pixel in the image. The simulated perfect mosaic was created by generating a quasi-symmetric hexagonal array. The dimensions of the array and pixel sampling were chosen to be similar to those found in real images. The spacing of the pseudocells across the image varied from 12 to 23 pixels, similar to the spacing found in the human and monkey images shown later. The simulated noisy mosaic was generated by convolving the simulated perfect mosaic with a 2D Gaussian function of 25×25 pixels in size and $\sigma = 3$ pixels to blur the edges of the simulated cells. Several randomized elliptical spots, of varying intensity, using a function described elsewhere [41], were also added to the image to simulate the structure of fluorescence seen in real images. Finally, a white Gaussian noise with SNR = 5 dB per sample was applied to add noise to the image; it was accomplished through the *awgn* MATLAB function.

C. Fluorescence AOSLO images

We used several different fluorescence AOSLO images obtained for current and previous experiments in the Center for Visual Science at the University of Rochester to test the algorithm. Images were obtained on three different fluorescence AOSLO systems. For comparison to manual cell counting measurements, we used images and measurements from a monkey RPE mosaic, published previously by Morgan and co-workers, using methods described previously [3,6,9]. This data set represents the largest and most well-characterized RPE mosaic imaged using fluorescence AOSLO. We compared the performance of the algorithm to the measurements obtained by Morgan *et al.* by using our algorithm to analyze the properties of the cell mosaic in the exact same areas for which they presented their data from the image shown in Fig. 1 and Table 1 of their paper [6]. Comparisons were made to the raw data, which we obtained from the authors. To compare performance on images of the RPE from the monkey that have somewhat different appearance (subjectively sharper, higher contrast, and less noisy), we used images obtained more recently by Masella *et al.* using similar methods but a smaller confocal aperture. We also evaluated the performance of the algorithm on images obtained recently from human eyes using methods we describe elsewhere [20]. Data shown from human participants are from experiments that were approved by the Research Subjects Review Board at the University of Rochester and adhered to the tenets of the

Table 1. Comparison of Algorithmic Segmentation and Manual Counting of RPE Cells in Monkey 320 from Morgan *et al.* [6]

Region ($^{\circ}$) ^a	Number of Cells ^b	Difference of Number of Cells ^c	Cell Density (cells/mm ²) ^b	Difference of Cell Density (cells/mm ²) ^c	Area Mean (μm^2) ^b	Difference of Area (μm^2) ^c	NND (μm) ^d
Fovea	211	30	4440	822	208	-18	13.33 \pm 1.51
1 T	230	4	4840	270	189	7	13.18 \pm 1.52
2 T	202	10	4250	273	224	-3	14.20 \pm 1.32
3 T	192	1	4040	209	227	8	14.63 \pm 1.47
4 T	181	1	3809	135	242	12	14.97 \pm 1.79
1 N	238	26	5008	697	178	-3	12.91 \pm 1.44
2 N	227	3	4777	301	192	5	13.42 \pm 1.40
3 N	204	19	4293	444	212	-4	13.81 \pm 1.70
4 N	179	21	3767	740	255	-34	14.68 \pm 1.97
1 S	234	30	4924	558	196	-13	13.26 \pm 1.72
2 S	218	34	4587	977	202	-22	13.27 \pm 1.62
3 S	198	42	4166	1147	209	-21	13.37 \pm 2.07
1 I	236	8	4966	267	184	7	13.10 \pm 1.36
2 I	221	16	4650	377	194	5	13.14 \pm 1.53
3 I	180	19	3788	1184	244	-42	13.87 \pm 2.15
1 T, 1 S	227	27	4777	694	196	-13	13.21 \pm 1.62
2 T, 2 S	193	17	4061	528	226	-8	14.25 \pm 1.69
3 T, 3 S	185	3	3893	197	249	-4	14.68 \pm 2.12
1 T, 1 I	243	6	5113	159	176	14	12.99 \pm 1.30
2 T, 2 I	180	31	3788	780	239	-21	14.55 \pm 1.76
3 T, 3 I	160	16	3367	570	277	-23	15.10 \pm 2.56
1 N, 1 S	216	28	4545	1182	203	-28	13.21 \pm 1.71
2 N, 2 S	214	26	4503	669	207	-14	13.55 \pm 1.81
3 N, 3 S	179	47	3767	988	238	-28	14.27 \pm 1.80
1 N, 1 I	240	28	5050	357	181	4	12.90 \pm 1.66
2 N, 2 I	195	24	4103	539	224	-9	13.77 \pm 1.65
3 N, 3 I	191	4	4019	728	221	-10	14.32 \pm 1.77

^aLocation of the center of the region as measured in degrees from the fovea in the direction temporal (T), nasal (N), superior (S), and inferior (I).

^bCalculated with the proposed algorithm.

^cDifference with respect to that reported in [6].

^dMean \pm SD.

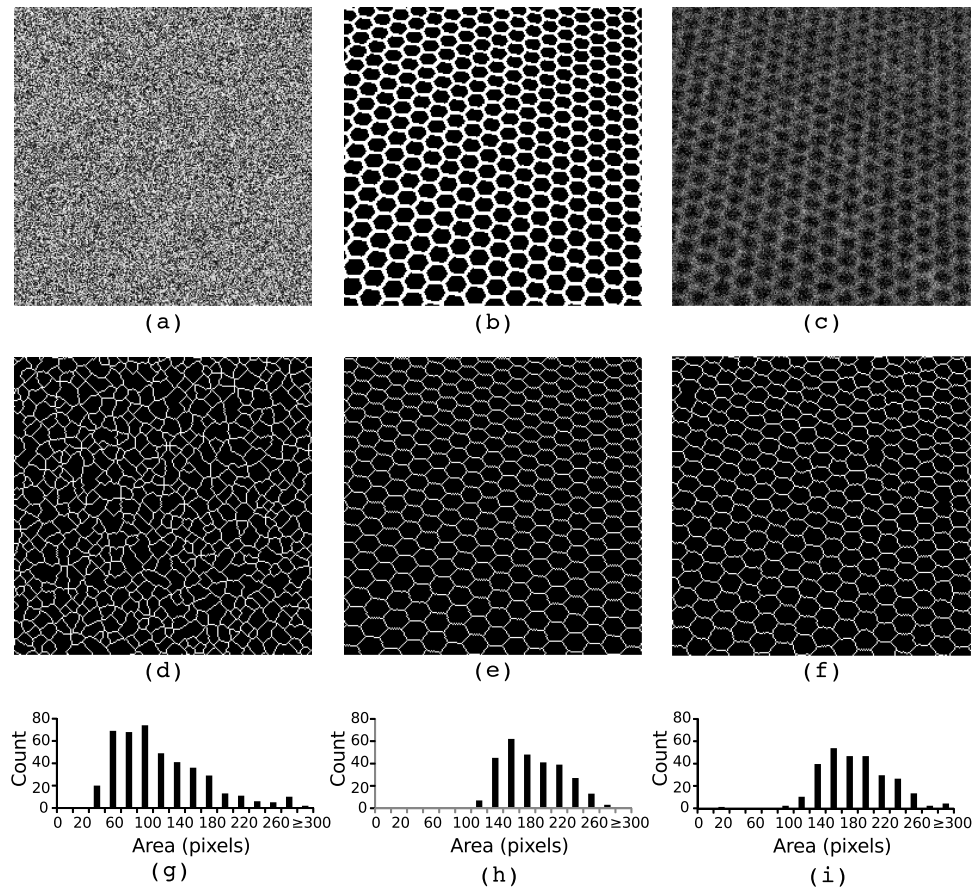


Fig. 4. Synthetic images (top row), corresponding segmentation images (middle row), and cell area histograms (bottom row). Histograms were generated from the cell areas computed from the segmentation images. (a), (d), (g) White noise, (b), (e), (h) hexagonal array, and (c), (f), (i) hexagonal array with SNR = 5 db. The pseudocells' diameters are between 12 and 24 pixels.

Declaration of Helsinki. Pixel dimensions were calculated by using a Gullstrand no. 2 simplified relaxed schematic eye model, scaled by the axial length of the eye.

To test the repeatability of the algorithm, we used images obtained in monkeys from the same retinal area, taken at different time points over the course of 1 h (~20 min between each video). Additionally, we wanted to see how varying the level of noise in real images altered algorithm performance. To examine this, we used images obtained at the same retinal location, but with different excitation source power levels. After image segmentation, the centroid and area were calculated for each cell; these parameters were used to calculate the cell area and nearest neighbor distance (NND).

3. RESULTS

Figure 4 shows the three different types of synthetic images in the first row, the result of the algorithm in the second row, and histograms of cell areas in the third row. For the case of the image containing no cellular structure (i.e., white noise) in Fig. 4(a), the algorithm produced the result shown in Fig. 4(d), which does not have the characteristic hexagonal appearance of a real RPE mosaic. The size and shape of the segmented regions vary in a random way, with the mean area = 109.7 pixels and standard deviation (SD) = 55.9 pixels. For the perfect simulated mosaic shown in Fig. 4(b), the algorithm correctly segmented all of the pseudocells in Fig. 4(e); the mean area was 176.4 pixels and the SD of area

was 36.7 pixels. For the noisy simulated mosaic shown in Fig. 4(c), the algorithm segmented almost all of the pseudocells (279/287 cells; 97.21%); in Fig. 4(f), the mean area was 177.5 pixels and the SD of area was 42.8 pixels. However, the algorithm failed to segment the pseudocell borders in four regions where the cell borders are poorly defined.

Figure 5 shows the results obtained on real images. For images shown in Figs. 5(a), 5(c), and 5(d), the Huang method was used to segment the blood vessel area. Figure 5(b) shows the RPE mosaic from the foveal center of monkey 320 from [5]. Statistical analysis of the segmented image shown in Fig. 5(b) is listed in the first row of Table 1. Table 1 also includes the statistics for the other 25 images (not shown) that we analyzed, which correspond to the areas measured in [6], as well as the difference between our measurements and those obtained by manual cell identification [6].

Figure 6 shows the results of the segmentation algorithm on three images of the same retinal area obtained at different time points. The number of cells found in each image varied by a maximum of 11 cells. Cell statistics computed from these areas (shown in Table 2) were similar. Figure 7 shows the results of the segmentation algorithm on the five images obtained using different excitation source power levels. Statistics for the segmented cells are shown in Table 2. Cell number decreased as excitation power increased for the four lowest power settings; a comparable number of cells were segmented in the two images obtained with the highest excitation source powers [Figs. 7(e) and 7(f)].

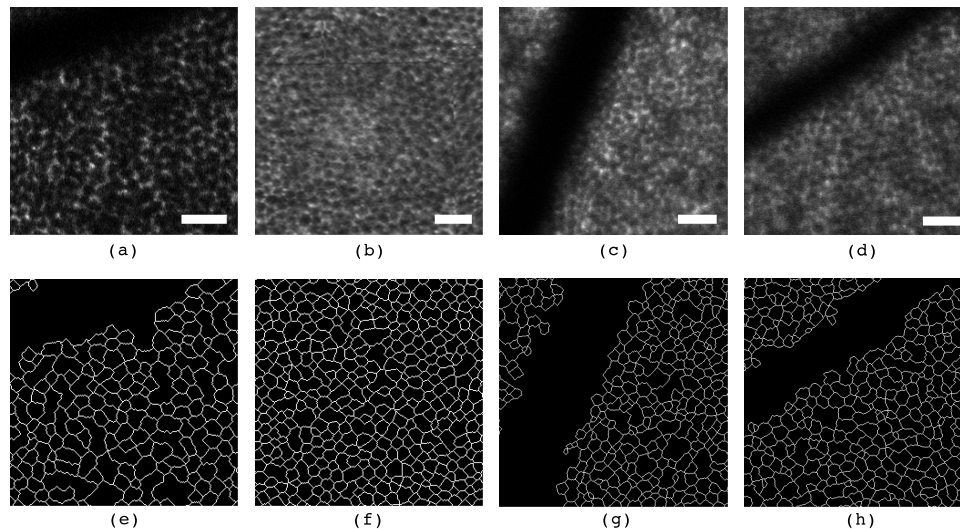


Fig. 5. RPE cells mosaic and corresponding segmentation: (a), (e) Monkey 526 at approximately 10° nasal-superior, (b), (f) monkey 320 at fovea, (c), (g) human at approximately 6.75° superior and 2.5° temporal, and (d), (h) human at approximately 1.75° superior and 10° temporal. Scale bar: $50\ \mu\text{m}$.

4. DISCUSSION

A. Performance on Simulated Images

The results from white noise show that, as with all image processing tools, care must be used in its application or spurious results can be obtained from noise. However, we feel that the results from the white noise example show that noise generates patterns that are very different, both qualitatively and quantitatively, from those obtained from either the simulated or real RPE mosaics and do not limit the utility of the algorithm. Qualitatively, it can be seen that the characteristic hexagonal mosaic is not observed in the white noise image.

Quantitatively, we can see from the area of the pseudocells plotted in the histogram in Fig. 4 that the noise image resulted in a skewed distribution of cell sizes, with a greater number of smaller cells (resulting in the smaller mean area reported above), and a long tail that extended into the larger bins. Results from the simulated perfect mosaic show that, as expected, for a perfect image, perfect segmentation occurs. The histogram of cell areas shows a normal distribution of cell areas about the area mean. Unfortunately, we do not expect to encounter such images in fluorescence AOSLO. Such high-contrast images are usually only obtained in confocal

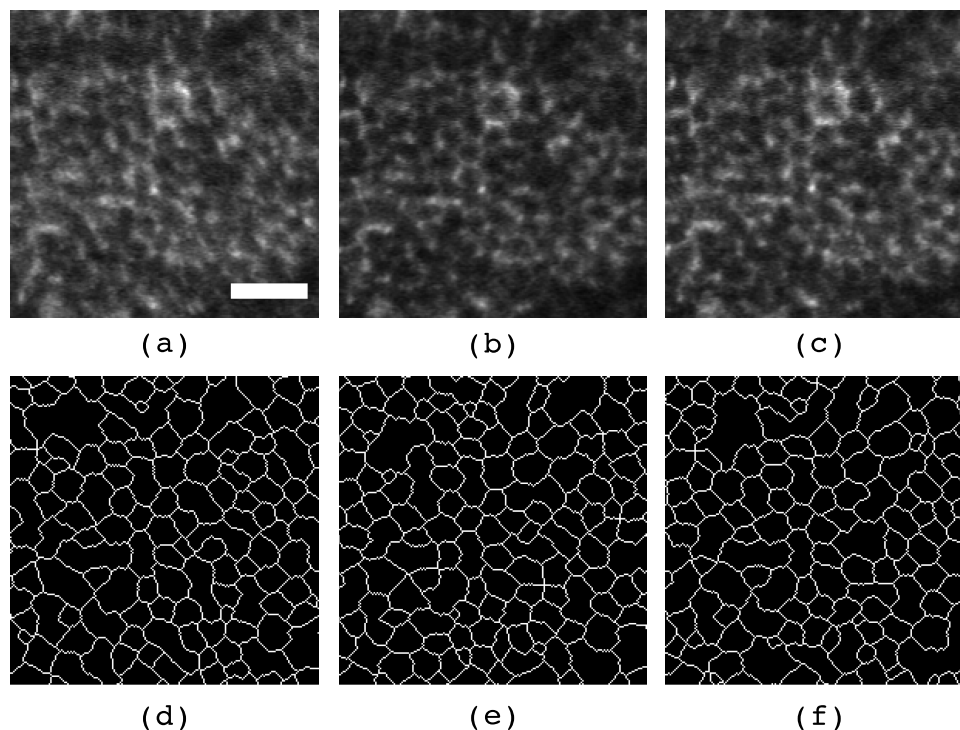


Fig. 6. Macaque RPE cells mosaic and corresponding segmentation at approximately 2° temporal, 7° superior: (a), (d) time point 1; (b), (e) time point 2; (c), (f) time point 3. Scale bar: $50\ \mu\text{m}$.

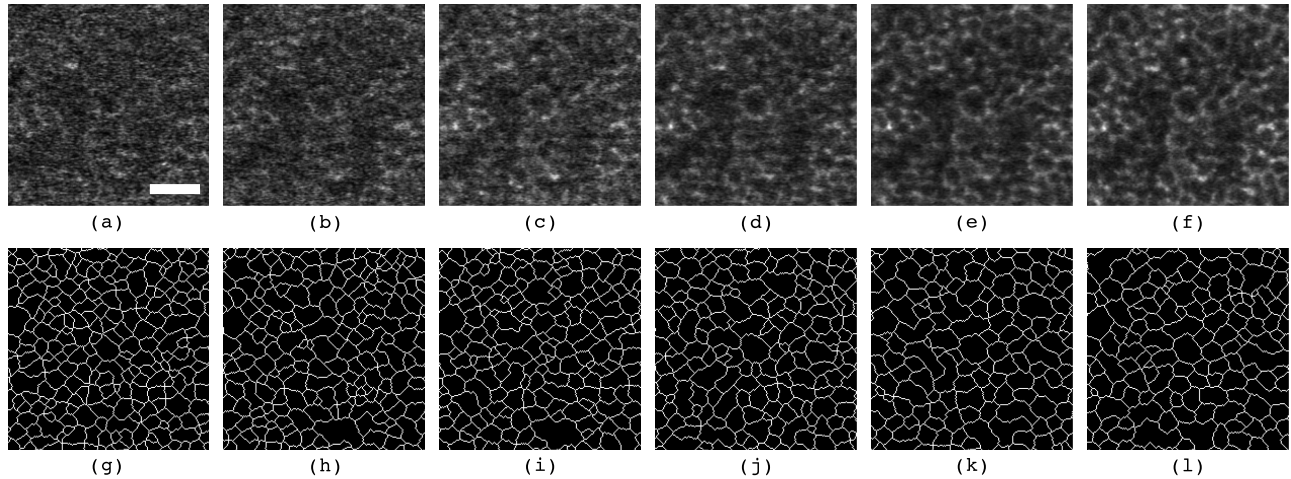


Fig. 7. Macaque RPE cells mosaic at different exposures and corresponding segmentation at approximately 2° temporal, 9° superior: (a), (g) $5 \mu\text{W}$, (b), (h) $12 \mu\text{W}$, (c), (i) $16 \mu\text{W}$, (d), (j) $20 \mu\text{W}$, (e), (k) $30 \mu\text{W}$, and (f), (l) $47 \mu\text{W}$. Scale bar: $50 \mu\text{m}$.

microscopy and can be segmented using other algorithms, such as the one proposed by Chiu *et al.* [23]. Results from the simulated noisy mosaic might represent a best-case imaging scenario. Here we see that as with most automated analysis tools there will be some errors even on the best images. In this case, we see that some pseudocells incorrectly have twice the area of the mean, representing two cells that were falsely identified as one. This occurs when the borders between two cells are indistinct; this case often arises in real images due to incomplete or nonuniform fluorescence along the cell margin. A few missed cells results in a negligible change in mean cell area, cell density, or NDD, and for most purposes these errors might be acceptable. However, when there is the expectation of a normal regular mosaic, these errors in segmentation could be automatically detected by computing the area of all of the cells and applying a threshold to determine those cells that are double or triple the mean size, representing two or three cells, respectively.

B. Performance on Real Images

Compared to manual cell identification, the algorithm found 19 fewer cells, on average, in the 26 locations examined for monkey 320 from [6]. At all locations compared, the algorithm segmented fewer cells than were identified manually. This discrepancy is due to algorithm failure in cases in which there was either incomplete fluorescence or hypo fluorescence of

the polygonal intensity signal that defines each cell. The algorithm fails when cell borders are not distinct, as it did in the simulated noisy mosaic image. However, if a border is completely missing, then it is not surprising that the algorithm fails to detect it. As stated in the introduction, RPE fluorescence of individual cells is variable and can depend on the spatial arrangement and state of the lipofuscin granules in the cell. In some cases, a border may be indistinct due to a lack of lipofuscin, or so hypo fluorescent that it cannot be detected by the algorithm. The result is the same in either case; multiple cells are segmented as one. The human brain is very good at inferring the presence of two cells despite an absent or indistinct border; thus the manual counts always identified more cells. This absolute systematic error between methods is demonstrated in the Bland–Altman plot shown in Fig. 8 [42].

One solution to this is to add an analysis step that computes the area of each cell and displays those cells that are greater than 2 SD above the mean to the experimenter, so that those cells may be segmented manually. However, overlaying the binary segmentation image on the original image in a software program such as Adobe Photoshop (Adobe Systems Inc., San Jose, California) or GIMP (GNU Image Manipulation Program) is usually all that is needed to identify cell margins that were not segmented; the pencil tool can then be used to trace the inferred cell border. Visual inspection of results and comparison to original imagery is important for any automated

Table 2. Statistics of RPE Cells from Monkey 526 in Figs. 6 and 7

Figure	Number of Cells ^a	Cell Density (cells/mm ²) ^a	Area Mean (μm^2) ^b	NND (μm) ^c
6(d)	138	3629	216.27	13.24 ± 3.44
6(e)	149	3918	204.76	13.12 ± 2.65
6(f)	143	3760	209.79	13.15 ± 3.01
7(g)	235	6180	121.34	10.05 ± 2.23
7(h)	205	5391	144.65	10.74 ± 2.45
7(i)	197	5180	146.90	10.74 ± 2.62
7(j)	189	4970	158.39	11.37 ± 2.69
7(k)	155	4076	196.91	12.71 ± 3.28
7(l)	149	3918	202.07	12.57 ± 3.05

^aCalculated with the proposed algorithm.

^bAverage area from cells.

^cMean \pm SD.

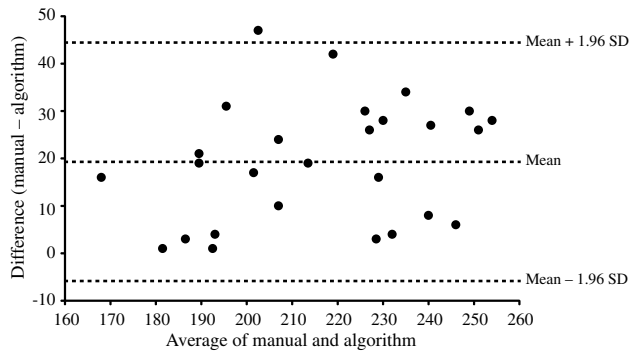


Fig. 8. Bland–Altman plot shows that there is an absolute systematic error between the proposed algorithm and manual cell identification. This is due to the fact that the human can infer the presence of two or more cells when their borders are indistinct or absent, but the algorithm cannot.

image analysis tool; just as the automated cone counting algorithms in use by investigators require manual correction, so too will that step be necessary for this tool.

Analysis of images obtained at the same retinal location at different time points (Fig. 6) showed that the algorithm is repeatable if the signal-to-noise ratio (SNR) of the images is similar. This is further demonstrated by the images shown in Fig. 7, as we see a similar number of cells segmented in the two images obtained with the highest excitation source power. Algorithm performance will suffer on noisier images, as is demonstrated from the results obtained using the lower power levels in Fig. 7.

C. Comparison to Manual Identification of Cell Centers

A major advantage of this approach is that it is much faster than manual identification. It took ~ 6 s to segment the entire RPE montage from Fig. 1 of [6]; this is ~ 6000 times faster than the 10 h it took Dr. Morgan to manually identify the 14,335

cells [43]. This savings in time can allow for many more images to be analyzed (even when adding time for manual correction), and will facilitate analysis of larger data sets than are manageable using purely manual methods. Now, the manual counts are slightly more accurate, in terms of identifying nearly every cell, as the trained eye can infer that a cell is there even if one of the borders is indistinct. However, it is clear that this level of precision is probably not necessary for some purposes, as similar cell statistics can be obtained (Table 1). A second and likely more important advantage of our approach is that this method provides more information; it not only obtains the information about where the cell is, but also allows other morphometric parameters to be computed. This may not be critical for evaluating the RPE mosaic in healthy young eyes, where a well-tessellated triangular packing is expected, but we feel it is essential for evaluating the structure of the RPE in diseased eyes [20]. Voronoi analysis can estimate these parameters for a well-tessellated area; however, there are some important differences between a Voronoi diagram and true cell segmentation. This is illustrated in Fig. 9, which compares the cells segmented in our simulated mosaic using our method to a Voronoi diagram of the same cells based upon the known center of each hexagon. Now, suppose some cells are lost—the cells shown in red in Fig. 9(a); the Voronoi diagram cannot faithfully represent this morphology [Fig. 9(c)]. However, our cell segmentation algorithm will correctly represent the shape of the areas defined by the remaining surrounding cells [Fig. 9(e)]. This is due to the fact that Voronoi domains must be convex. This results in the spurious triangles that now appear at the location of the missing cell in the corresponding Voronoi diagram shown in Fig. 9(c). Even more problematic is representing patches of cell loss or RPE cells that might be surrounded by several lost cells. This is illustrated by the simulated RPE mosaic shown in Fig. 9(h): the Voronoi diagram is incomplete, with most of the domains

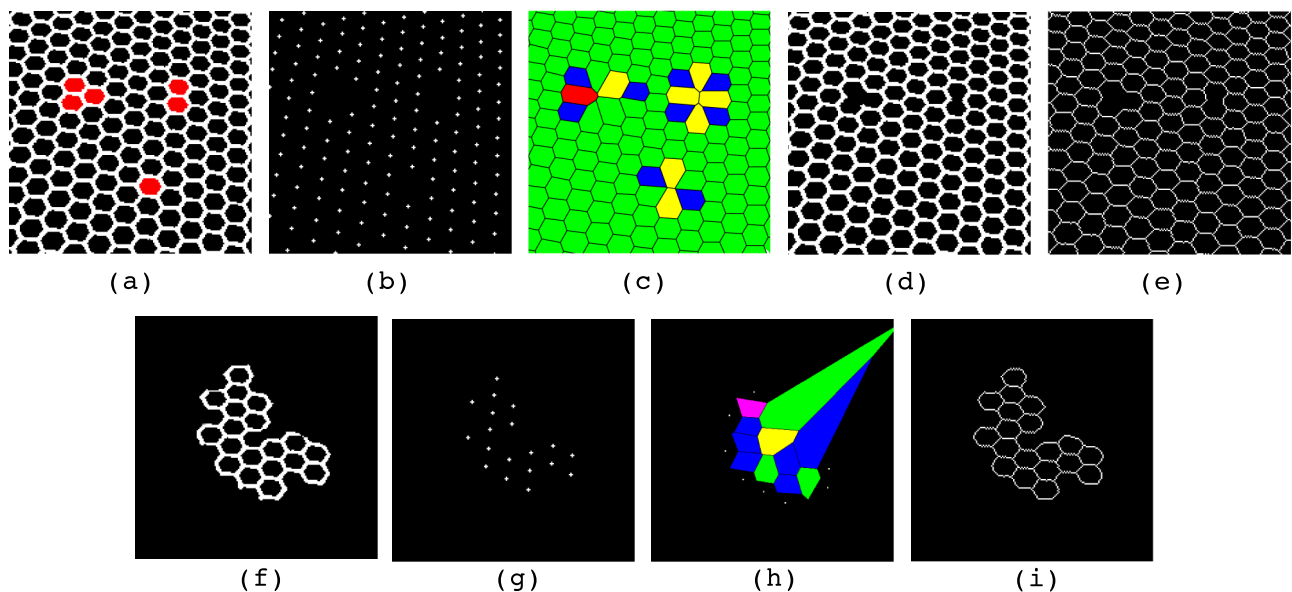


Fig. 9. Comparison of cells segmentation using Voronoi diagram and the proposed algorithm. (a) Simulated RPE mosaic supposing lost cells in red, (b) centroids from (a), (c) Voronoi diagram from (b), (d) simulated mosaic with lost cells, (e) segmentation from (d) using proposed algorithm, (f) simulated RPE mosaic surrounded by several lost cells, (g) centroids from (f), (h) Voronoi diagram from (g), and (i) segmentation from (f) using proposed algorithm. Magenta, blue, green, yellow, and red synthetic cells have 4, 5, 6, 7, and 8 Voronoi neighbors, respectively.

unable to be filled as the surrounding area is devoid of points. Since the edges of a Voronoi diagram are defined by the points that bound it, and in this case there are no bounding points, it fails to represent the data faithfully. Again, we see that the proposed algorithm [Fig. 9(i)] will faithfully represent this morphology [Fig. 9(f)] when the Voronoi method fails.

ACKNOWLEDGMENTS

The authors thank Jessica Morgan, Ph.D., for sharing her images and cell counting data with us. We also thank Ben Masella, Ph.D., and Jennifer J. Hunter, Ph.D., for sharing their images with us. This work was supported by NIH grants F32EY021669, EY014375, EY004367, EY021786, and EY001319; a postdoctoral award to Ethan A. Rossi, Ph.D., from Fight for Sight (FFS-PD-11-020); and Research to Prevent Blindness. We also acknowledge the support of *Consejo Nacional de Ciencia y Tecnología* (CONACyT) through grant 162031 and projects 166326 and 166070.

REFERENCES

- J. Liang, D. R. Williams, and D. T. Miller, "Supernormal vision and high-resolution retinal imaging through adaptive optics," *J. Opt. Soc. Am. A* **14**, 2884–2892 (1997).
- A. Roorda, F. Romero-Borja, I. William Donnelly, H. Queener, T. Hebert, and M. Campbell, "Adaptive optics scanning laser ophthalmoscopy," *Opt. Express* **10**, 405–412 (2002).
- D. C. Gray, W. Merigan, J. I. Wolfing, B. P. Gee, J. Porter, A. Dubra, T. H. Twietmeyer, K. Ahamd, R. Tumbar, F. Reinholz, and D. R. Williams, "In vivo fluorescence imaging of primate retinal ganglion cells and retinal pigment epithelial cells," *Opt. Express* **14**, 7144–7158 (2006).
- R. C. Baraas, J. Carroll, K. L. Gunther, M. Chung, D. R. Williams, D. H. Foster, and M. Neitz, "Adaptive optics retinal imaging reveals s-cone dystrophy in tritan color-vision deficiency," *J. Opt. Soc. Am. A* **24**, 1438–1447 (2007).
- J. Carroll, S. S. Choi, and D. R. Williams, "In vivo imaging of the photoreceptor mosaic of a rod monochromat," *Vis. Res.* **48**, 2564–2568 (2008).
- J. I. W. Morgan, A. Dubra, R. Wolfe, W. H. Merigan, and D. R. Williams, "In vivo autofluorescence imaging of the human and macaque retinal pigment epithelial cell mosaic," *Investig. Ophthalmol. Vis. Sci.* **50**, 1350–1359 (2008).
- J. J. Hunter, B. Masella, A. Dubra, R. Sharma, L. Yin, W. H. Merigan, G. Palczewski, K. Palczewski, and D. R. Williams, "Images of photoreceptors in living primate eyes using adaptive optics two-photon ophthalmoscopy," *Biomed. Opt. Express* **2**, 139–148 (2011).
- A. Dubra and Y. Sulai, "Reflective afocal broadband adaptive optics scanning ophthalmoscope," *Biomed. Opt. Express* **2**, 1757–1768 (2011).
- E. A. Rossi, M. Chung, A. Dubra, J. J. Hunter, W. H. Merigan, and D. R. Williams, "Imaging retinal mosaics in the living eye," *Eye* **25**, 301–308 (2011).
- D. R. Williams, "Imaging single cells in the living retina," *Vis. Res.* **51**, 1379–1396 (2011).
- J. I. W. Morgan, J. J. Hunter, B. Masella, R. Wolfe, D. C. Gray, W. H. Merigan, F. C. Delori, and D. R. Williams, "Light-induced retinal changes observed with high-resolution autofluorescence imaging of the retinal pigment epithelium," *Investig. Ophthalmol. Vis. Sci.* **49**, 3715–3729 (2008).
- D. T. Miller, D. R. Williams, G. M. Morris, and J. Liang, "Images of cone photoreceptors in the living human eye," *Vis. Res.* **36**, 1067–1079 (1996).
- O. Strauss, "The retinal pigment epithelium in visual function," *Physiol. Rev.* **85**, 845–881 (2005).
- D. Bok, "The retinal pigment epithelium: a versatile partner in vision," *J. Cell Sci., Suppl.* **17**, 189–195 (1993).
- P. Kay, Y. Yang, and L. Paraoan, "Directional protein secretion by the retinal pigment epithelium: roles in retinal health and the development of age-related macular degeneration," *J. Cell. Mol. Med.* **17**, 833–843 (2013).
- A. Rashid, S. K. Arora, M. A. Chrenek, S. Park, Q. Zhang, J. M. Nickerson, and H. E. Grossniklaus, "Spatial analysis of morphometry of retinal pigment epithelium in the normal human eye," presented at ARVO 2013 Annual Meeting, Seattle, Washington, 2013.
- A. Roorda, Y. Zhang, and J. L. Duncan, "High-resolution in vivo imaging of the RPE mosaic in eyes with retinal disease," *Investig. Ophthalmol. Vis. Sci.* **48**, 2297–2303 (2007).
- E. A. Rossi, D. R. Williams, A. Dubra, L. R. Latchney, M. A. Folwell, W. Fischer, H. Song, and M. M. Chung, "Individual retinal pigment epithelium cells can be imaged in vivo in age related macular degeneration," presented at ARVO 2013 Annual Meeting, Seattle, Washington, 2013.
- C. K. Dorey, G. Wu, D. Ebenstein, A. Garsd, and J. J. Weiter, "Cell loss in the aging retina. Relationship to lipofuscin accumulation and macular degeneration," *Investig. Ophthalmol. Vis. Sci.* **30**, 1691–1699 (1989).
- E. A. Rossi, P. Rangel-Fonseca, K. Parkins, W. Fischer, L. R. Latchney, M. Folwell, D. Williams, A. Dubra, and M. M. Chung, "In vivo imaging of retinal pigment epithelium cells in age related macular degeneration," *Biomed. Opt. Express* **4**, 2527–2539 (2013).
- D. Scoles, Y. N. Sulai, and A. Dubra, "In vivo dark-field imaging of the retinal pigment epithelium cell mosaic," *Biomed. Opt. Express* **4**, 1710–1723 (2013).
- K. Y. Li and A. Roorda, "Automated identification of cone photoreceptors in adaptive optics retinal images," *J. Opt. Soc. Am. A* **24**, 1358–1363 (2007).
- S. J. Chiu, C. A. Toth, C. B. Rickman, J. A. Izatt, and S. Farsiu, "Automatic segmentation of closed-contour features in ophthalmic images using graph theory and dynamic programming," *Biomed. Opt. Express* **3**, 1127–1140 (2012).
- S. J. Chiu, Y. Likhnygina, A. M. Dubis, A. Dubra, J. Carroll, J. A. Izatt, and S. Farsiu, "Automatic cone photoreceptor segmentation using graph theory and dynamic programming," *Biomed. Opt. Express* **4**, 924–937 (2013).
- S. K. Arora, A. Rashid, M. A. Chrenek, Q. Zhang, S. Park, H. E. Grossniklaus, and J. M. Nickerson, "Analysis of human retinal pigment epithelium (RPE) morphometry in the macula of the normal aging eye," presented at ARVO 2013 Annual Meeting, Seattle, Washington, 2013.
- L. V. Del Priore, Y.-H. Kuo, and T. H. Tezel, "Age-related changes in human RPE cell density and apoptosis proportion in situ," *Investig. Ophthalmol. Vis. Sci.* **43**, 3312–3318 (2002).
- M. Boulton and P. Dayhaw-Barker, "The role of the retinal pigment epithelium: topographical variation and ageing changes," *Eye* **15**, 384–389 (2001).
- Y. N. Sulai and A. Dubra, "Adaptive optics scanning ophthalmoscopy with annular pupils," *Biomed. Opt. Express* **3**, 1647–1661 (2012).
- N. M. Putnam, D. X. Hammer, Y. Zhang, D. Merino, and A. Roorda, "Modeling the foveal cone mosaic imaged with adaptive optics scanning laser ophthalmoscopy," *Opt. Express* **18**, 24902–24916 (2010).
- M. O. M. Ts'o and E. Friedman, "The retinal pigment epithelium: I. Comparative histology," *Arch. Ophthalmol.* **78**, 641–649 (1967).
- D. M. Snodderly, M. M. Sandstrom, I. Y.-F. Leung, C. L. Zucker, and M. Neuringer, "Retinal pigment epithelial cell distribution in central retina of rhesus monkeys," *Investig. Ophthalmol. Vis. Sci.* **43**, 2815–2818 (2002).
- R. C. Gonzalez and R. E. Woods, *Digital Image Processing* (Addison-Wesley, 1993).
- J. C. Russ, *The Image Processing Handbook* (CRC Press, 2002).
- J. P. Serra, *Image Analysis and Mathematical Morphology* (Academic, 1982).
- H. Wilson and S. Giese, "Threshold visibility of frequency gradient patterns," *Vis. Res.* **17**, 1177–1190 (1977).
- D. Marr and E. Hildreth, "Theory of edge detection," *Proc. R. Soc. B* **207**, 187–217 (1980).
- S. Beucher and F. Meyer, "Methodes d'analyse de contrastes a l'analyseur de textures," Technical report (Ecole des Mines

- de Paris, Centre de Morphologie Mathématique Fontainebleau, 1977).
38. L.-K. Huang and M.-J. J. Wang, "Image thresholding by minimizing the measures of fuzziness," *Pattern Recogn.* **28**, 41–51 (1995).
 39. G. W. Zack, W. E. Rogers, and S. A. Latt, "Automatic measurement of sister chromatid exchange frequency," *J. Histochem. Cytochem.* **25**, 741–753 (1977).
 40. N. Otsu, "A threshold selection method from gray-level histograms," *IEEE Trans. Syst. Man Cybern.* **9**, 62–66 (1979).
 41. J. C. Valencia-Estrada and A. H. Bedoya-Calle, "Trigonometría elíptica para su uso en ingeniería," in *Jornadas de Investigación EIA 2009* (Escuela de Ingeniería de Antioquia, 2009), pp. 84–92.
 42. J. M. Bland and D. G. Altman, "Statistical methods for assessing agreement between two methods of clinical measurement," *Lancet* **327**, 307–310 (1986).
 43. J. I. W. Morgan, Department of Ophthalmology, University of Pennsylvania, 3400 Civic Center Blvd., Ophthalmology 3rd floor WEST 3–113W, Philadelphia, Pennsylvania 19104–6100 (personal communication, 2013).